JOURNAL OF SOLID STATE CHEMISTRY 102, 79–92 (1993)

Neutron Diffraction Study of High Ionic Conductor $Rb_4Cu_{16}I_{7+x}Cl_{13-x}$ at 50–300 K: Correlation with Ionic Conductivity

R. KANNO,* K. OHNO, AND Y. KAWAMOTO

Department of Chemistry, Faculty of Science, Kobe University, Kobe, Hyogo, 657 Japan

Y. TAKEDA AND O. YAMAMOTO

Department of Chemistry, Faculty of Engineering, Mie University, Tsu, Mie, 514 Japan

T. KAMIYAMA AND H. ASANO

Institute of Materials Science, University of Tsukuba, Tsukuba, Ibaraki, 305 Japan

F. IZUMI

National Institute for Research in Inorganic Materials, Tsukuba, Ibaraki, 305 Japan

AND S. KONDO

Department of Research and Development Technology Laboratory, Matsushita Battery Industrial Company Ltd., Moriguchi, Osaka, 570 Japan

Received November 18, 1991; in revised form May 22, 1992; accepted May 28, 1992

The high ionic conductor $Rb_4Cu_{16}I_{7+x}Cl_{13-x}$ was characterized by electrical conductivity, X-ray diffraction, and neutron diffraction measurements. The compositions $Rb_4Cu_{16}I_7Cl_{13}$ and $Rb_4Cu_{16}I_{7.2}Cl_{12.8}$ were synthesized using a solid-state reaction at 403 K. Arrhenius conductivity plots showed smooth slope changes at 150–300 K, corresponding to a so-called diffuse phase transition. $Rb_4Cu_{16}I_{7.2}Cl_{12.8}$ showed slightly higher conductivities above 200 K, whereas no significant difference was found below 200 K. The structural parameters of $Rb_4Cu_{16}I_{7.2}Cl_{12.8}$ were refined by Rietveld analysis of TOF neutron diffraction data at 50–300 K. In three sets of Cu sites, a gradual migration of copper ions from the Cu(3) site into the Cu(2) site was observed in the temperature range 110 to 300 K, which corresponds to the migration of nonconducting copper ions into the conduction pathways. All the structural changes proceed gradually over a wide range of temperature, 110–300 K; this corresponds exactly to the temperatures where the conductivity curves showed smooth slope changes.

* Author to whom correspondence should be addressed.

0022-4596/93 $5.00

Introduction

The high ionic conductor $Rb_4Cu_{16}I_7Cl_{13}$ found by Takahashi *et al.* has a room-temperature conductivity of 0.34 S/cm, which is the highest conductivity value of the ionic conductors so far prepared (*1*). $Rb_4Cu_{16}I_7Cl_{13}$ is, therefore, a technologically important material as an electrolyte for all solid-state batteries (*2*); its high ionic conductivity makes it possible to mix polymer binder and to fabricate a thin-film electrolyte without significant conductivity degradation (*3*). Thin-film solid-state batteries using this electrolyte and copper Chevrel anode and cathode showed extraordinary high charge–discharge current densities of several mA/cm^2 (*4*). On the other hand, its electric properties are of intrinsic interest, since its high ionic conductivity is attained without showing a large and discontinuous change in Arrhenius conductivity plots, which seems to correspond to a higher-order phase transition (*1*, *5*).

The transition from normal conduction state to high conduction state is of particular interest for understanding the conduction mechanism of a high ionic conductor. The transitions were previously studied and divided into two or three categories, for example, (i) normal solids, (ii) materials showing first-order transition, and (iii) materials showing higher-order transition before its high conduction state (*6*). The transition of the third category is sometimes called a diffuse phase transition, which is found in many high ionic conductors such as β-PbF_2 (*7*), halide spinels (*8*), and $PyAg_5I_6$ (*9*).

The transitions from normal to high conduction state are extensively studied, for example, in high-temperature fluorites. The transition temperature, however, exceeds 1000 K (*7*), which is beyond the working temperature of the experimental apparatus commonly used. The anomaly in the conductivity plots for $Rb_4Cu_{16}I_7Cl_{13}$ was observed around room temperature (*1*, *5*), which is much lower than those observed in the high-temperature fluorites. This makes $Rb_4Cu_{16}I_7Cl_{13}$ experimentally a favorable model system for understanding the disorder, diffuse phase transition, and transport mechanism in high conduction states.

Phase transitions in $Rb_4Cu_{16}I_7Cl_{13}$ reported previously are, however, considerably confused; Takahashi *et al.* indicated a break in the conductivity curve at 248 K (*1*), whereas Geller *et al.* reported two breaks in the conductivity curve at 170 and 221 K, corresponding to γ–(170 K) $\rightarrow$ β–(221 K) $\rightarrow$ α phase transitions (*5*). Rong-Jian *et al.*, on the other hand, indicated one phase transition at 259 K (*10*), and three transitions were reported at 247, 223, and 163 K by Zong-Yuan *et al.* (*11*). More recently, Turkovic *et al.* reported a broad heat anomaly around 150 K for $RbCu_4I_{1.665}Cl_{3.335}$ in DSC measurements (*12*). The difference in the phase transitions might be due partly to the sample preparation conditions; a systematic study based on synthesis, structural analysis, conductivity, and specific heat measurements has yet to be carried out to clarify the phase relation below room temperature and the mechanism of the high ionic conductivity of $Rb_4Cu_{16}I_7Cl_{13}$.

We report here the structural changes from low temperatures to room temperature using neutron diffraction measurements, together with the ionic conductivity data. The results on specific heat measurements will also be published elsewhere (*13*).

Experimental

Anhydrous copper chloride (CuCl), copper iodide (CuI), and rubidium chloride (RbCl) were used (Nakarai Company, >99.9% purity). CuCl was purified by recrystallization from hydrochloric acid. The recrystallized copper(I) chloride was completely dried under vacuum at 400 K; then it was stored in an evacuated Pyrex tube. CuI and RbCl were used after drying care-

fully under vacuum (~1 Pa) at 400 K without further purification. The appropriate quantities of the starting materials were weighed and ground together with an agate mortar in a glove box. Then pellets of the samples pressed under 90 MPa were heated at 407 K in an evacuated Pyrex tube. The grinding and annealing cycle were repeated until no change in the X-ray diffraction pattern of the product was observed.

Electrical conductivities of 0.5-g pressed pellets were measured in the temperature range 77 to 473 K in a dry argon gas flow. Blocking gold electrodes were deposited on both sides of the pellets by evaporation. The conductivity was obtained by ac impedance measurement with a Solartron 1250 frequency response analyzer over a frequency range of 0.1 and 65×10^3 Hz. Resistances were derived by interpretation of the complex impedance plane diagram of the data.

X-Ray diffraction (XRD) patterns of the powdered samples were obtained using a high-power XR diffractometer (Rigaku RAD 12kW) with monochromated Cu$K\alpha$ radiation and a scintillation detector. The diffraction data were collected between 77 and 400 K for 2 sec at each 0.02° step width over a 2θ range from 20° to 100°. The lattice parameters were refined by Rietveld analysis using the computer program RIETAN (*14*). Reflection positions and intensities were calculated for both Cu$K\alpha_1$ and Cu$K\alpha_2$, with a factor of 0.5 applied to the latter's calculated integrated intensities. A pseudo-Voigt profile function was used; the mixing parameter γ was included in the least-squares refinement.

Neutron diffraction data were taken on a high-resolution TOF neutron powder diffractometer, HRP (*15*), at the KENS pulsed spallation neutron source at the National Laboratory for High Energy Physics (KEK). The specimen was contained in a cylindrical vanadium cell 5 mm in radius, 42 mm in height, and 100 μm in thickness. The scattering angle, 2θ, was fixed at 170°, and intensity data were collected at 50, 110, 220, and 300 K with a gate width of 4–16 μsec.

Results and Discussion

Synthesis

The composition of the electrolyte was given as $Rb_4Cu_{16}I_7Cl_{13}$ by Takahashi *et al.* (*1*). On the other hand, Geller *et al.* concluded from structural studies that the stoichiometric material was actually $RbCu_4I_2Cl_3$, but a nonstoichiometric composition could be prepared of the type $RbCu_4Cl_{3+y}I_{2-y}$ ($0.0 \leq y \leq 0.4$) (*5*). When $y = 0.25$ the composition is equivalent to the formula given by Takahashi *et al.* Although a wide solid solution range was proposed, Takahashi *et al.* reported the range of $-0.2 \leq x \leq 0.5$ in $Rb_4Cu_{16}I_{7+x}Cl_{13-x}$, when prepared at 403–413 K (*16*), and Tokumoto *et al.* also reported the range of $0.125 \leq y \leq 0.25$ in $RbCu_4I_{2-y}Cl_{3+y}$ ($0.0 \leq x \leq 0.5$ in $Rb_4Cu_{16}I_{7+x}Cl_{13-x}$) (*17*).

More recently, Geller *et al.* proposed the composition and stability of this compound as follows (*18*). Stoichiometric $RbCu_4I_2Cl_3$ is thermodynamically stable in the narrow temperature range 473 ± 15 K, and the materials with $0.02 \leq y \leq 0.40$ ($-0.6 \leq x \leq 0.92$ in $Rb_4Cu_{16}I_{7+x}Cl_{13-x}$) appear to be stable from at least 78 K to their preparation temperatures which depend on x. Further, the stoichiometric $RbCu_4I_2Cl_3$ can be converted by cold work to a low-symmetry phase with the probable composition $RbCu_4I_{1.96}Cl_{3.04}$ ($Rb_4Cu_{16}I_{7.84}Cl_{12.16}$). It transforms rapidly to the cubic phase with a formula $RbCu_4I_{1.96}Cl_{3.04}$ at temperatures above 348 K.

The stability was also determined by electrochemical measurements. Polarization measurement of $Rb_4Cu_{16}I_{7+x}Cl_{13-x}$ using the cell $Cu/Rb_4Cu_{16}I_{7+x}Cl_{13-x}/Cu$ revealed an increase in anodic polarization with x, which indicates that the material with higher chloride content is more stable in contact with copper metal and thermodynamically stable at room temperature (*19*). Kleitz *et al.* (*20*)

reported for the samples prepared at 463–473 K that the best conductivity value was obtained for $RbCu_4Cl_3I_2$ at room temperature but the complex impedance analysis using Cu metal or copper Chevrel phase $Cu_2Mo_6S_8$ revealed a marked instability toward lower values. The conductivity of $RbCu_4I_{1.75}Cl_{3.25}$ ($Rb_4Cu_{16}I_7Cl_{13}$) was 0.36 S/cm and was stable.

The previous results have thus been summarized as follows. The compositional range was $-0.6 \leq x \leq 1.0$ in $Rb_4Cu_{16}I_{7+x}Cl_{13-x}$ when prepared at 473 K and $-0.2 \leq x \leq 0.5$ when prepared at 403 K. The compositions near $Rb_4Cu_{16}I_7Cl_{13}$ are thermodynamically stable at room temperature. Solid-state cells using this composition show the high performances with high current density at a wide range of working temperatures (*2*, *4*).

In the present study, we synthesized the compositions $Rb_4Cu_{16}I_7Cl_{13}$ and $Rb_4Cu_{16}I_{7.2}Cl_{12.8}$, which are in the range of solid solution $-0.2 \leq x \leq 0.5$ in $Rb_4Cu_{16}I_{7+x}Cl_{13-x}$. The reaction was repeated at 403 K and no change in diffraction pattern of the products was observed after five repetitions. The lattice parameters were calculated to be 10.0107(1) and 10.0134(2) Å, respectively, which are consistent with the reported values (*16*).

Electrical Conductivity Measurements

Figure 1 shows the temperature dependence of the conductivity of $Rb_4Cu_{16}I_7Cl_{13}$ and $Rb_4Cu_{16}I_{7.2}Cl_{12.8}$ between 125 and 400 K. There are clearly curving regions at 150–300 K; above 300 K, the activation energies were calculated to be about 10 kJ/mole, which is characteristic of a high conduction state. No evidence of a first-order transition was observed in these conductivity curves.

Below 200 K, there are no significant differences in conductivities between $Rb_4Cu_{16}I_7Cl_{13}$ and $Rb_4Cu_{16}I_{7.2}Cl_{12.8}$, whereas $Rb_4Cu_{16}I_{7.2}Cl_{12.8}$ shows slightly higher conductivities than $Rb_4Cu_{16}I_7Cl_{13}$ above 200 K. The fact that $Rb_4Cu_{16}I_{7.2}Cl_{12.8}$ has higher ionic conductivity than $Rb_4Cu_{16}I_7Cl_{13}$ is consistent with the results on heat capacity measurements (*13*); i.e., an abnormal increase was observed in the heat capacity curves above 90 K. When the excess heat capacities of $Rb_4Cu_{16}I_7Cl_{13}$ and $Rb_4Cu_{16}I_{7.2}Cl_{12.8}$ were compared, the latter had a slightly higher value, with a maximum at a slightly higher temperature, than the former. The larger excess heat capacity of $Rb_4Cu_{16}I_{7.2}Cl_{12.8}$ implies that the Cu ions should be more mobile in the crystal.

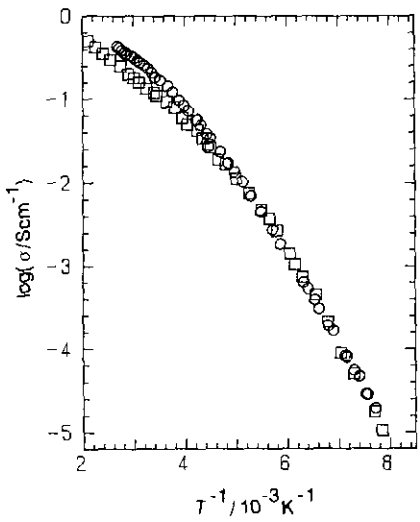

FIG. 1. Temperature dependence of the conductivity for $Rb_4Cu_{16}I_7Cl_{13}$(□) and $Rb_4Cu_{16}I_{7.2}Cl_{12.8}$ (○).

We previously measured conductivities using a mixture of $Rb_4Cu_{16}I_{7+x}Cl_{13-x}$ and copper metal electrodes (*16*), which has caused decomposition of the electrolyte. The decomposition proceeded faster for the samples with higher iodide content, leading to slightly higher conductivities for $Rb_4Cu_{16}I_7Cl_{13}$ than $Rb_4Cu_{16}I_{7.2}Cl_{12.8}$. However, the measurements using sputtered Au electrode have led to higher conductivities for $Rb_4Cu_{16}I_{7.2}Cl_{12.8}$, which is consistent with the previ-

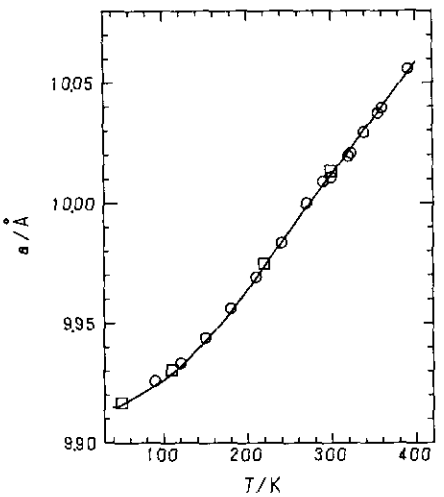

FIG. 2. Temperature dependence of the lattice parameter for $Rb_4Cu_{16}I_7Cl_{13}$ (○) determined by X-ray diffraction measurement and for $Rb_4Cu_{16}I_{7.2}Cl_{12.8}$ (□) determined by neutron diffraction measurement.

ous results reported by Kleitz *et al.* (*20*) and Geller *et al.* (*21*).

X-Ray Diffraction Measurements

The X-ray diffraction patterns between 77 and 473 K were indexed by the cubic cell with space groups $P4_332$ or $P4_132$, and no significant change was observed in the diffraction patterns. The gradual slope change in the conductivity curve was, therefore, not accompanied by a symmetry change. Geller *et al.* have determined the crystal structure of $RbCu_4I_2Cl_3$ by single-crystal X-ray analysis at room temperature (*5*). The compound has either $P4_332$ or $P4_132$ space group with a unit-cell dimension $a = 10.032(3)$ Å. The lattice parameters were therefore refined by the Rietveld method using this structural model. Refinement proceeded to an agreement factor R_I less than 10% at all temperatures. Figure 2 shows the temperature dependence of the lattice parameter. A slight slope change is observed above 150 K, which corresponds to the anomaly in the conductivity–temperature curve.

Neutron Diffraction Measurements

Intensity data for interplanar spacings between 0.5 and 3.4 Å were used for Rietveld analysis, but those in TOF regions—18,299–18,759, 22,769–22,849, 25,909–26,167, 29,911–30,431 μsec at 50 K, 18,329–18,769, 21,069–21,299, 25,899–26,050, 30,171–30,418 μsec at 110 K, 18,429–18,879, 19,849–20,039, 21,089–21,219, 26,052–26,232 μsec at 220 K, and 18,479–18,949, 19,959–20,129, 30,483–30,704 μsec at 300 K—were excluded in the refinement owing to the appearance of very weak peaks due to CuI. No significant changes in diffraction patterns were observed between 50 and 300 K. Refinement of the structure therefore proceeded with space group $P4_132$ with the structural model reported for $RbCu_4I_2Cl_3$ (*5*). The excess Cl in $Rb_4Cu_{16}I_{7.2}Cl_{12.8}$ was assumed to occupy the 8*c* site with a Cl : I ratio of 0.1 : 0.9. The site occupation parameters *g* for the Cu(1), Cu(2), and Cu(3) sites were refined using isotropic thermal parameters and a constraint that the total number of Cu atoms is fixed at a starting composition.

When the temperature factors for the sites were allowed to be anisotropic, the refinement was unstable. The occupation factors were fixed at values obtained by the refinement using isotropic thermal parameters, and then the anisotropic thermal parameters were refined for sites which have large isotropic thermal parameters, the Cu(1) and Cu(2) sites at 110 and 220 K and the Cu(1) site at 300 K. No correction for preferred orientation was made.

Table I lists final *R* factors (*22*), lattice and structural parameters, and their standard deviations. Table II gives interatomic distances calculated with ORFFE (*23*). Figure 3 illustrates the profile fit and difference patterns for $Rb_4Cu_{16}I_{7.2}Cl_{12.8}$. The solid lines are calculated intensities, dots overlying them are observed intensities, and Δy_i is the difference between observed and calculated intensities. Figure 3 shows that the calcu-

TABLE I

STRUCTURAL PARAMETERS FOR $Rb_4Cu_{16}I_{7.2}Cl_{12.8}$ IN $P4_132$

Atom	Site	g	x	y	z	B/Å^2
A. T = 50 K, a = 9.9167(2) Å, R_{wp} = 3.80%, R_p = 2.92%, R_e = 3.80%, R_I = 5.13%, R_F = 3.03%						
Rb	$4a(\frac{3}{8}, \frac{3}{8}, \frac{3}{8})$	1.0	$\frac{3}{8}$	$\frac{3}{8}$	$\frac{3}{8}$	0.64(4)
Cu(1)	$24e(x, y, z)$	0.341(3)	0.5203(3)	0.2948(3)	0.8045(3)	1.03(7)
Cu(2)	$24e(x, y, z)$	0.260(3)	0.0011(5)	0.8314(5)	0.1967(5)	1.35(11)
Cu(3)	$8c(x, x, x)$	0.195	0.1654(5)	$=x$	$=x$	0.9(3)
I	$8c(x, x, x)$	0.9	0.01121(13)	$=x$	$=x$	0.40(3)
Cl(1)	$8c(x, x, x)$	0.1	0.01121	$=x$	$=x$	0.40
Cl(2)	$12d(\frac{1}{8}, y, y + \frac{1}{4})$	1.0	$\frac{1}{8}$	0.14952(6)	$=y + \frac{1}{4}$	0.45(2)
B. T = 110 K, a = 9.9305(1) Å, R_{wp} = 3.17%, R_p = 2.50%, R_e = 3.01%, R_I = 4.63%, R_F = 2.96%						
Rb	$4a(\frac{3}{8}, \frac{3}{8}, \frac{3}{8})$	1.0	$\frac{3}{8}$	$\frac{3}{8}$	$\frac{3}{8}$	1.06(6)
Cu(1)	$24e(x, y, z)$	0.342[a]	0.5214(4)	0.2935(5)	0.8043(4)	1.76[b]
Cu(2)	$24e(x, y, z)$	0.260[a]	0.0020(5)	0.8338(6)	0.1993(5)	1.98[b]
Cu(3)	$8c(x, x, x)$	0.190[a]	0.1673(5)	$=x$	$=x$	0.61(19)
I	$8c(x, x, x)$	0.9	0.01148(14)	$=x$	$=x$	0.65(4)
Cl(1)	$8c(x, x, x)$	0.1	0.01148	$=x$	$=x$	0.65
Cl(2)	$12d(\frac{1}{8}, y, y + \frac{1}{4})$	1.0	$\frac{1}{8}$	0.14957(7)	$=y + \frac{1}{4}$	0.67(2)

Atom	U_{11}/Å^2	U_{22}/Å^2	U_{33}/Å^2	U_{12}/Å^2	U_{13}/Å^2	U_{23}/Å^2
Cu(1)	0.006(2)	0.049(3)	0.011(2)	−0.003(2)	0.0064(18)	0.001(2)
Cu(2)	0.003(2)	0.045(4)	0.025(4)	0.007(2)	0.007(2)	0.001(3)

C. T = 220 K, a = 9.9748(1) Å, R_{wp} = 2.78%, R_p = 2.18%, R_e = 2.88%, R_I = 4.91%, R_F = 3.83%						
Rb	$4a(\frac{3}{8}, \frac{3}{8}, \frac{3}{8})$	1.0	$\frac{3}{8}$	$\frac{3}{8}$	$\frac{3}{8}$	1.96(7)
Cu(1)	$24e(x, y, z)$	0.344[a]	0.5217(3)	0.2920(6)	0.8013(5)	3.96[b]
Cu(2)	$24e(x, y, z)$	0.278[a]	0.0039(5)	0.8406(7)	0.2104(5)	3.73[b]
Cu(3)	$8c(x, x, x)$	0.130[a]	0.1635(8)	$=x$	$=x$	1.6(3)
I	$8c(x, x, x)$	0.9	0.01110(13)	$=x$	$=x$	0.88(4)
Cl(1)	$8c(x, x, x)$	0.1	0.01110	$=x$	$=x$	0.88
Cl(2)	$12d(\frac{1}{8}, y, y + \frac{1}{4})$	1.0	$\frac{1}{8}$	0.15014(6)	$=y + \frac{1}{4}$	1.14(3)

Atom	U_{11}/Å^2	U_{22}/Å^2	U_{33}/Å^2	U_{12}/Å^2	U_{13}/Å^2	U_{23}/Å^2
Cu(1)	0.007(2)	0.096(4)	0.046(3)	0.007(2)	0.013(2)	0.016(3)
Cu(2)	0.011(2)	0.076(5)	0.053(4)	0.026(3)	0.018(2)	0.026(4)

D. T = 300 K, a = 10.0134(2) Å, R_{wp} = 2.85%, R_p = 2.23%, R_e = 3.19%, R_I = 5.69%, R_F = 5.49%						
Rb	$4a(\frac{3}{8}, \frac{3}{8}, \frac{3}{8})$	1.0	$\frac{3}{8}$	$\frac{3}{8}$	$\frac{3}{8}$	2.66(5)
Cu(1)	$24e(x, y, z)$	0.342[a]	0.5213(2)	0.2921(3)	0.7968(3)	5.81[b]
Cu(2)	$24e(x, y, z)$	0.287[a]	0.0008(3)	0.8407(4)	0.2110(3)	4.06(8)
Cu(3)	$8c(x, x, x)$	0.110[a]	0.1643(6)	$=x$	$=x$	3.00
I	$8c(x, x, x)$	0.9	0.01107(9)	$=x$	$=x$	1.46(3)
Cl(1)	$8c(x, x, x)$	0.1	0.01107	$=x$	$=x$	1.46
Cl(2)	$12d(\frac{1}{8}, y, y + \frac{1}{4})$	1.0	$\frac{1}{8}$	0.15057(4)	$=y + \frac{1}{4}$	1.57(2)

TABLE I—*Continued*

Atom	U_{11}/Å^2	U_{22}/Å^2	U_{33}/Å^2	U_{12}/Å^2	U_{13}/Å^2	U_{23}/Å^2
Cu(1)	0.0146(18)	0.135(3)	0.070(3)	0.026(2)	0.0138(19)	0.028(2)

[a] The occupation factors at Cu(1), Cu(2), and Cu(3) sites were fixed at values obtained by the refinement using isotropic thermal parameters. These values for Cu(1), Cu(2), and Cu(3) sites were as follows: 0.342(4), 0.260(4), 0.190 at 110 K; 0.344(5), 0.278(5), 0.130 at 220 K; 0.342(5), 0.287(5), 0.110 at 300 K. Numbers in parentheses are estimated standard deviations of the last significant digit, and those without deviations were fixed by the constraint that the total number of Cu atoms is 16 in the unit cell.

[b] Equivalent thermal parameters, B_{eq}.

TABLE II

INTERATOMIC DISTANCES AND ANGLES OF Rb AND Cu ENVIRONMENTS FOR $Rb_4Cu_{16}I_{7.2}Cl_{12.8}$[a]

	Distance, d (Å)			
	50 K	110 K	220 K	300 K
Cu(1)–Cu(1^{i})	1.668(8)	1.674(9)	1.723(10)	1.805(6)
Cu(1)–Cu(2^{ii})	1.660(4)	1.655(5)	1.623(6)	1.599(3)
Cu(1)–Cu(2^{iii})	1.522(7)	1.505(8)	1.402(7)	1.397(3)
Cu(1)–Cu(3^{iv})	1.521(4)	1.526(5)	1.523(5)	1.546(3)
Cu(1)–Cl(2^{v})	2.340(4)	2.340(4)	2.330(4)	2.305(3)
Cu(1)–Cl(2^{iv})	2.417(3)	2.405(5)	2.419(6)	2.451(3)
Cu(1)–I^{vi} or Cl(1^{vi})	2.664(4)	2.672(4)	2.683(4)	2.684(2)
Cu(1)–I^{v} or Cl(1^{v})	2.654(3)	2.665(4)	2.714(5)	2.755(3)
Cu(2)–Cl(2^{vii})	2.394(5)	2.429(7)	2.545(8)	2.542(4)
Cu(2)–Cl(2^{viii})	2.410(5)	2.395(5)	2.325(4)	2.313(3)
Cu(2)–I^{ix} or Cl(1^{ix})	2.539(5)	2.532(5)	2.525(5)	2.563(3)
Cu(2)–I^{viii} or Cl(1^{vii})	2.563(4)	2.569(5)	2.617(5)	2.632(3)
Cu(3)–Cl(2)	2.361(3)	2.350(4)	2.394(6)	2.402(5)
Cu(3)–I, Cl(1)	2.648(9)	2.680(9)	2.634(14)	2.658(11)
Rb–Cl(2)	3.3474(4)	3.3517(4)	3.3634(4)	3.3738(3)
	Angle, θ (deg)			
Cu(1^{i})–Cu(1)–Cu(2^{ii})	101.3(3)	100.3(4)	96.7(4)	97.0(2)
Cu(1^{i})–Cu(1)–Cu(2^{iii})	114.6(2)	114.6(2)	115.7(2)	115.42(19)
Cu(1^{i})–Cu(1)–Cu(3^{iv})	107.6(3)	108.0(3)	104.7(4)	101.9(3)
Cu(1)–Cu(2^{iii})–Cu(1^{x})	110.1(3)	111.5(4)	119.3(4)	120.8(2)
Cu(2^{ii})–Cu(1)–Cu(2^{iii})	108.7(2)	109.4(3)	115.0(3)	117.48(18)
Cu(2^{ii})–Cu(1)–Cu(3^{iv})	116.2(4)	116.3(4)	120.7(6)	119.8(4)
Cu(2^{iii})–Cu(1)–Cu(3^{iv})	108.2(3)	108.0(3)	103.8(4)	104.2(3)

[a] Coordinate triplets: (i) $-y + \frac{3}{4}, -x + \frac{3}{4}, -z + \frac{7}{4}$; (ii) $-x + \frac{1}{2}, -y + 1, z + \frac{1}{2}$; (iii) z, x, y; (iv) $x + \frac{1}{2}, -y + \frac{1}{2}, -z + 1$; (v) $y + \frac{1}{2}, -z + \frac{1}{2}, -x + 1$; (vi) $z + \frac{1}{4}, -y + \frac{1}{4}, x + \frac{3}{4}$; (vii) $-x, y + \frac{1}{2}, -z + \frac{1}{2}$; (viii) $-y + \frac{1}{4}, x + \frac{3}{4}, z + \frac{1}{4}$; (ix) $-y, z + \frac{1}{2}, -x + \frac{1}{2}$; (x) $z - \frac{1}{4}, y + \frac{1}{4}, -x + \frac{3}{4}$.

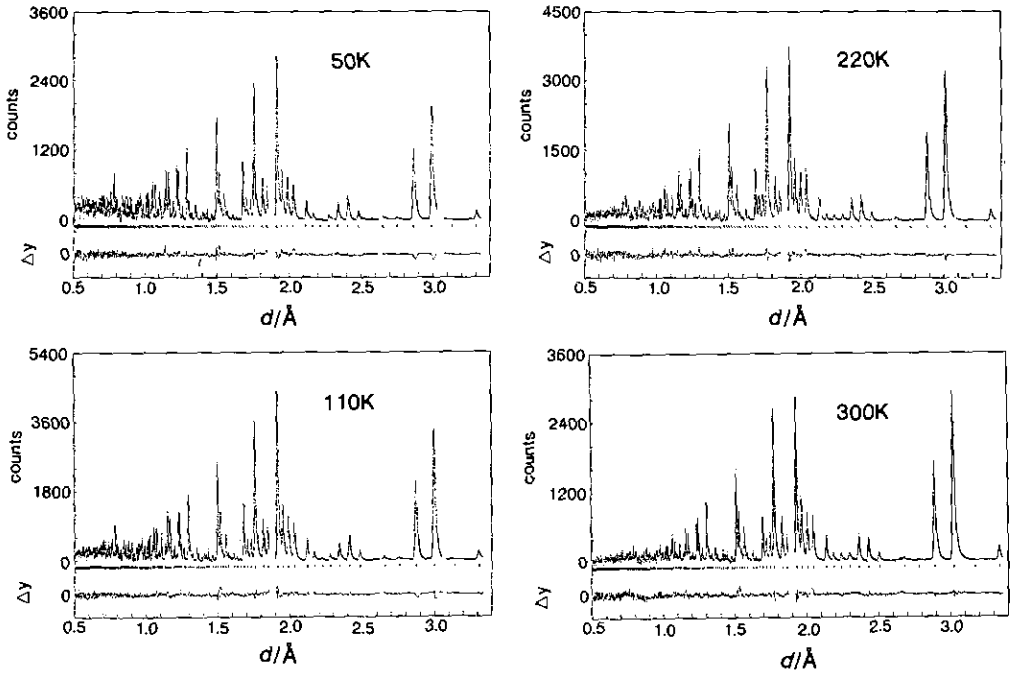

FIG. 3. Observed, calculated, and difference plots for the Rietveld analysis.

lated pattern fits the observed one very well. The lattice parameters at each temperature are plotted in Fig. 2, together with those obtained by X-ray diffraction measurements, indicating that these parameters are in good agreement with each other. An idealized ORTEP-II drawing of the structure for $Rb_4Cu_{16}I_{7.2}Cl_{12.8}$ is illustrated in Figs. 4 and 5.

The occupancies were determined at 300 K to be 0.342(5), 0.287(5), and 0.110 for Cu(1), Cu(2), and Cu(3), respectively. These values are consistent with the reported values for $RbCu_4I_2Cl_3$ (5): 0.339(20), 0.294(17), and 0.132(24). Figure 6 shows the temperature dependence of the site occupation factors in Cu(1), Cu(2), and Cu(3) sites. At 50 K, the occupancies are 0.341(3), 0.260(3), and 0.195, respectively. Above 110 K, the occupancy at the Cu(3) site decreases from 0.190 (110 K) to 0.110 (300 K) and that at the Cu(2) site increases from 0.260(4) (110 K) to 2.875(5) (300 K).

Figure 7 shows the temperature dependence of the isotropic thermal parameter B for Cu(1), Cu(2), and Cu(3) sites. The thermal parameters for Cu(1), Cu(2), and Cu(3)

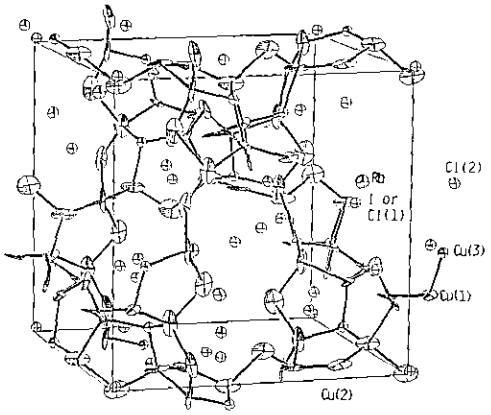

FIG. 4. Structure of $Rb_4Cu_{16}I_{7.2}Cl_{12.8}$ at 110 K. Thermal ellipsoids with 70% probability are drawn in the figure.

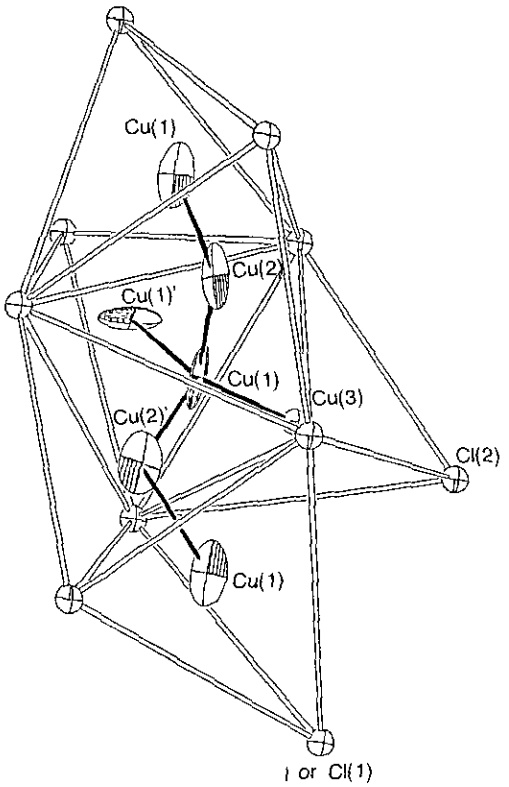

FIG. 5. Conduction pathways of $Rb_4Cu_{16}I_{7.2}Cl_{12.8}$ at 110 K. Cu(1)', Cu(2), and Cu(2)' indicate Cu(1^{i}), Cu(2^{ii}), and Cu(2^{iii}) in Table II, respectively.

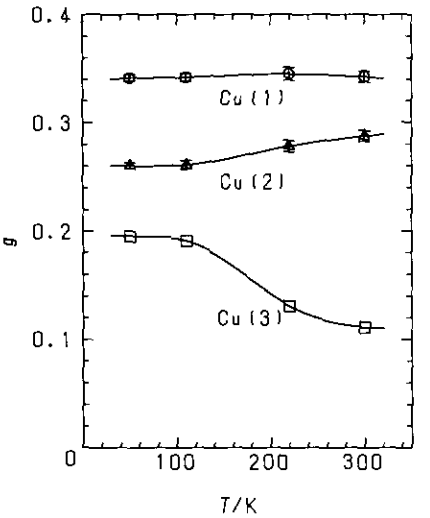

FIG. 6. Temperature dependence of site occupancies at Cu(1), Cu(2), and Cu(3) sites.

sites increase considerably with increasing temperature, whereas those for Rb, Cl, and I sites increase from around 0.5 Å^2 at 50 K to 1.5–2.5 Å^2 at 300 K (see Table I). The large increase in the parameters for Cu(1) and Cu(2) sites indicates a gradual migration of the copper ions above 100 K to those sites which probably participate significantly in the ionic conduction process.

Figure 8 shows the temperature dependence of the interatomic distances and angles. The most interesting features of these figures are the Cu–Cu variations. The Cu(1)–Cu(2)' and Cu(1)–Cu(2) interatomic distances decrease significantly with increasing temperature for $110 \leq T \leq 220$ K. On the other hand, the Cu(1)–Cu(1)' interatomic distances increase with temperature for $110 \leq T \leq 300$ K, and Cu(1)–Cu(3) distances vary little over the whole temperature range examined. The interatomic angles shown in Fig. 8d vary in the temperature range $110 \leq T \leq 300$ K. For example, the angles, Cu(1)–Cu(2)–Cu(1) and Cu(2)–

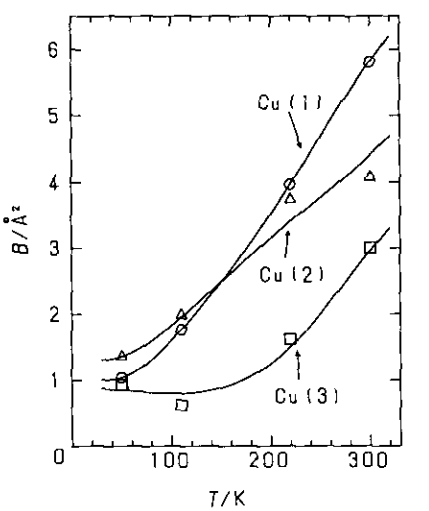

FIG. 7. Temperature dependence of the isotropic thermal parameters at Cu(1), Cu(2), and Cu(3) sites.

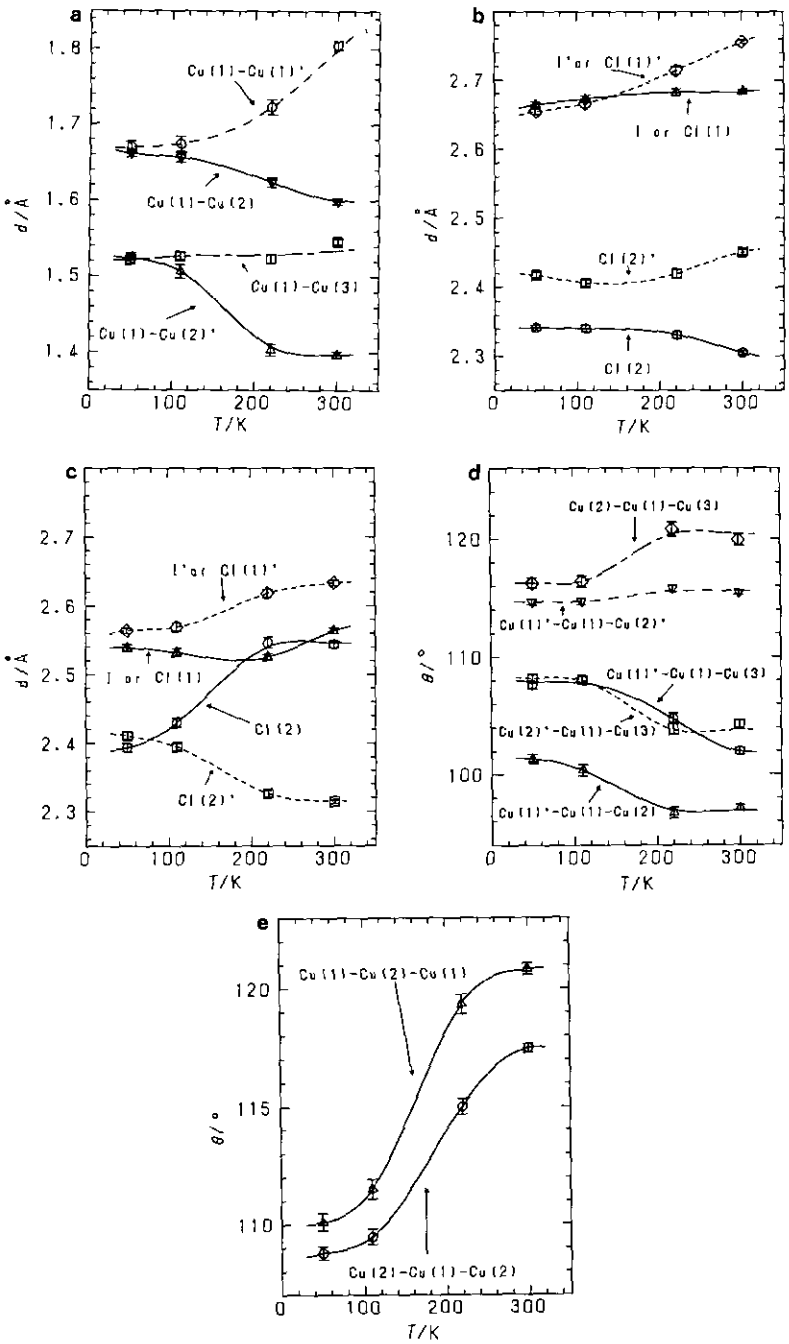

FIG. 8. (a) Temperature dependence of the Cu–Cu interatomic distances. Cu(1)', Cu(2), and Cu(2)' indicate Cu(1^{i}), Cu(2^{ii}) and Cu(2^{iii}) in Table II, respectively. (b) Temperature dependence of the Cu(1)–X interatomic distances. (c) Temperature dependence of the Cu(2)–X interatomic distances. (d, e) Temperature dependence of the interatomic angles.

Cu(1)–Cu(2), increase with temperature from 110° to 121° and from 109° to 117°, respectively.

$Rb_4Cu_{16}I_{7.2}Cl_{12.8}$ is basically isostructural to $RbAg_4I_5$ (*24*). In $Rb_4Cu_{16}I_{7.2}Cl_{12.8}$, there are essentially three sets of crystallographically nonequivalent sites for the Cu atoms, one 8-fold set [Cu(3)] and two 24-fold sets [Cu(1) and Cu(2)], making a total of 56 sites for 16 Cu atoms per unit cell. As shown in Table I, the atoms are not distributed at random over these sites. For a uniform distribution, the fractional occupancy is 0.286.

Possible conduction pathways are indicated previously as follows (*5*, *24*). A copper ion in a Cu(1) site may move through faces shared by tetrahedra to four neighboring sites, namely, the Cu(3) site, another Cu(1) site, or one of two Cu(2) sites. A copper ion in a Cu(2) site may move only to two Cu(1) sites through shared tetrahedron faces. The remaining two tetrahedron faces give access only to the Rb^+ ion which would repeal the Cu^+ ion. A copper ion in a Cu(3) site may move to one of three Cu(1) sites in neighboring tetrahedra which share faces with the tetrahedron about the Cu(3) site. The fourth face of the Cu(3) tetrahedron is shared with the Rb^+ octahedron. Alternating Cu(1) and Cu(2) sites form channels parallel to the three unit-cell axes. There are two such channels perpendicular to each unit-cell face. The Cu(3) site helps to connect these channels.

The structure refinement results in $Rb_4Cu_{16}I_{7.2}Cl_{12.8}$ over the temperature range $50 \leq T \leq 300$ K are summarized as follows. With increasing temperature, (1) the occupancy at the Cu(3) site decreases and that at the Cu(2) site increases; (2) the Cu(1)–Cu(2) and Cu(1)–Cu(2)′ interatomic distances decrease; (3) the Cu(2)–Cu(1)–Cu(2)′ and Cu(1)–Cu(2)–Cu(1) angles increase; and (4) the Cu(1)–Cu(1)′ interatomic distances increase. The large increase in the thermal parameters for Cu(1) and Cu(2) sites, shown in Fig. 7, suggests that these sites participate in the ionic conduction. This is consistent with the interatomic distance and angle variations obtained. The Cu–Cu distances along the conduction pathways decrease and the bend in the zig-zag conduction pathways along these tetrahedra decreases with increasing temperature. The –Cu(1)–Cu(2)–Cu(1)– conduction pathways connect with each other through Cu(1)–Cu(1)′ or Cu(1)–Cu(3)–Cu(1) pathways. However, the Cu(1)–Cu(3) and the Cu(1)–Cu(1)′ distances increase with temperature, which suggests that the copper ion migration through those sites does not contribute significantly to the total conduction in the structure. A gradual migration of copper ions from the Cu(3) into the Cu(2) site with increasing temperature corresponds to the migration of nonconducting copper ions in the Cu(3) site to the –Cu(1)–Cu(2)–Cu(1)– conduction pathways. All the structural changes proceed gradually over a wide range of temperatures, 110–300 K; this corresponds exactly to the range where the conductivity curves showed a smooth slope change. Figure 9 displays the $Z = 0.0$ sections of $|F_{obs}|$ Fourier syntheses computed using structure factors derived from these final refinements of the 110 and 220 K data. Substantial scattering density corresponding to copper is apparent at 220 K, indicating copper diffusion along the Cu(1) and Cu(2) sites.

Heat capacity measurement using a high-precision adiabatic calorimeter showed that an abnormal increase is observed in the heat capacity curve above 90 K, and that the heat capacity value exceeds the classical limit value of $12R = 998\ J\ K^{-1}\ mol^{-1}$ above 130 K (*13*). The excess heat capacity showed a broad anomaly with a maximum at about 190 K, which reveals a noncooperative mechanism for the redistribution of Cu ions in the crystal sites. The anomaly of the excess heat capacity corresponds to the remarkable variation in the occupancy of the 8-fold Cu(3) site as shown by the neutron diffraction.

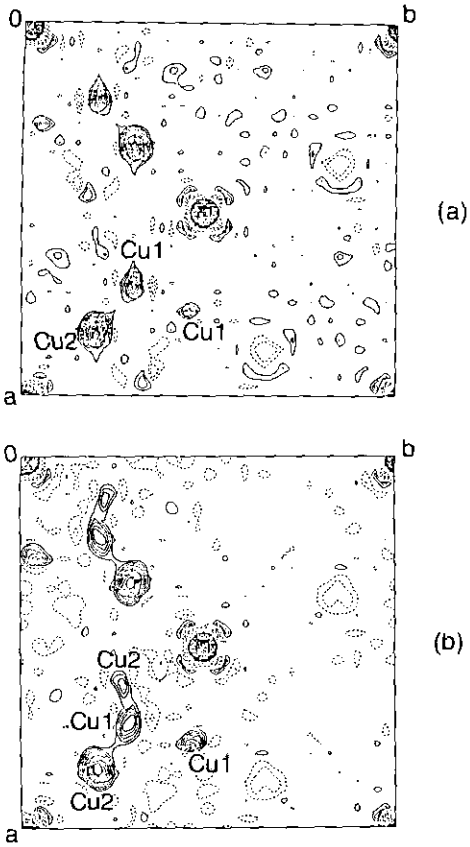

FIG. 9. $Z = 0.0$ sections of $|F_{obs}|$ Fourier syntheses calculated using structure factors derived from the final refinements of $Rb_4Cu_{16}I_{7.2}Cl_{12.8}$ at (a) 110 K and (b) 220 K.

Madelung Potential

We have calculated the Madelung potential (or the electrostatic energy required to bring a hole from infinity to each atomic site) for $Rb_4Cu_{16}I_{7.2}Cl_{12.8}$ using the program LATTEN (*25*). The site occupancy at each Cu site might closely be related to its site potential calculated from the neighbors. The Ewald summation method (*26*) was used for evaluation of the Madelung potentials. The results on Cu(1), Cu(2), and Cu(3) sites are summarized in Fig. 10. Madelung site potentials of Cu(3) sites are larger than those of Cu(1) and Cu(2) sites. The site potential increases with temperature particularly from 110 to 300 K. The temperature dependence of the site energy is also consistent with the site occupancy curves shown in Fig. 6. In both cases, gradual changes in curves are observed at 110–300 K.

Conclusions

We synthesized the high ionic conductor with compositions $Rb_4Cu_{16}I_7Cl_{13}$ and $Rb_4Cu_{16}I_{7.2}Cl_{12.8}$, using a solid-state reaction at 403 K. The compositions are in the range of solid solution $-0.2 \leq x \leq 0.5$ in $Rb_4Cu_{16}I_{7+x}Cl_{13-x}$ reported previously (*16*). The X-ray diffraction and neutron diffraction measurements between 50 and 400 K indicated no significant changes in diffraction patterns. The electrical conductivity was measured between 77 and 400 K. Arrhenius conductivity plots showed a curving region at 150–300 K and no evidence of a first-order transition. $Rb_4Cu_{16}I_{7.2}Cl_{12.8}$ had slightly higher conductivities above 200 K, whereas no significant difference was found below 200 K. This is consistent with the results on specific heat measurements (*13*); $Rb_4Cu_{16}I_{7.2}Cl_{12.8}$ had a slightly higher excess heat capacity, with a maximum at a slightly higher temperature, then $Rb_4Cu_{16}I_7Cl_{13}$.

The structure of $Rb_4Cu_{16}I_{7.2}Cl_{12.8}$ was determined using the Rietveld method for neutron diffraction data at 50, 110, 220, and 300 K. In the structure, there are essentially three sets of crystallographically nonequivalent sites for the Cu atoms, one 8-fold set [Cu(3)] and two 24-fold sets [Cu(1) and Cu(2)], making a total of 56 sites for 16 Cu atoms per unit cell. At 50 K, the occupancies are 0.341(3), 0.260(3), and 0.195, for Cu(1), Cu(2), and Cu(3) sites, respectively. Above 110 K, the occupancy at Cu(3) sites decreases gradually from 0.190 (110 K) to 0.110 (300 K) and that at Cu(2) sites increases from 0.260(4) (110 K) to 0.287(5) (300 K). The gradual occupation factor

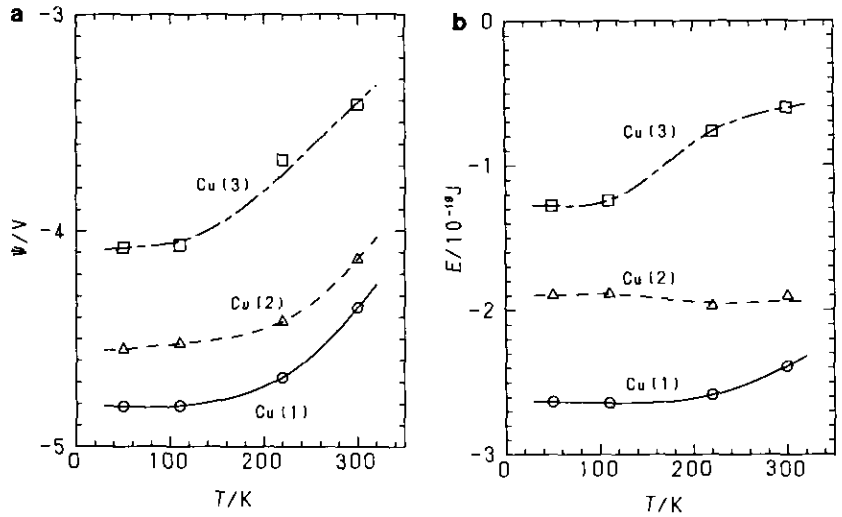

FIG. 10. Temperature dependence of the site potential (a) and site energy (b) at Cu(1), Cu(2), and Cu(3) sites.

changes correspond exactly to the curving region in Arrhenius conductivity plots.

Other structural changes above 110 K are summarized as follows. (i) The thermal parameters in Cu(1) and Cu(2) sites increase, (ii) the Cu(1)–Cu(2) and Cu(1)–Cu(2)′ interatomic distances decrease, (iii) the Cu(2)–Cu(1)–Cu(2)′ and Cu(1)–Cu(2)–Cu(1) angles increase, and (iv) the Cu(1)–Cu(1)′ interatomic distances increase with temperature. The Cu–Cu distances along the conduction pathways (–Cu(1)–Cu(2)–Cu(1)–) decrease and the bend in the zig-zag conduction pathways along these tetrahedra decreases with increasing temperature. Other pathways, e.g., Cu(1)–Cu(3)–Cu(1), do not contribute significantly to the total conduction in the structure. A gradual migration of copper ions from the Cu(3) to the Cu(2) site with increasing temperature corresponds to the migration of nonconducting copper ions in the Cu(3) site to the –Cu(1)–Cu(2)–Cu(1)– conduction pathways. All the structural changes proceed gradually over a wide range of temperatures, 110–300 K; this corresponds exactly to the temperature ranges when the conductivity curves showed gradual slope changes.

Acknowledgments

The authors thank Professor T. Atake for valuable discussions. All computations for structure determination were carried out at the Kobe University Information Processing Center.

References

1. T. TAKAHASHI, O. YAMAMOTO, S. YAMADA, AND S. HAYASHI, *J. Electrochem. Soc.* **126,** 1654 (1979).
2. R. KANNO, Y. TAKEDA, M. IMURA, AND O. YAMAMOTO, *J. Appl. Electrochem.* **12,** 681 (1982); R. Kanno, Y. Takeda, Y. Oda, H. Ikeda, and O. Yamamoto, *Solid State Ionics* **18/19,** 1068 (1986); R. Kanno, Y. Takeda, M. Ohya, and O. Yamamoto, *Mater. Res. Bull.* **22,** 1283 (1987).
3. K. TAKADA, T. KANBARA, T. SOTOMURA, AND S. KONDO, *in* "Symposium on Solid State Ionics, Tottori, Japan," p. 93 (1987); N. Yasuda, M. Nagata, S. Kondo, and T. Sotomura, "40th *ISE* Meeting Extended Abstracts, Kyoto, Japan," p. 1261 (1989).
4. T. SOTOMURA, Y. MORIWAKI, S. KONDO, AND T. IWAKI, "40th ISE Meeting Extended Abstracts, Kyoto, Japan," p. 1260 (1989); T. SOTOMURA, S. ITOH, S. KONDO, AND T. IWAKI, *Denki Kagaku* **59,** 129 (1991).

5. S. Geller, J. R. Akridge, and S. A. Wilber, *Phys. Rev.* **19,** 5396 (1979).
6. M. O'Keeffe, B. G. Hyde, *Philos. Mag.* **33,** 219 (1976); M. O'Keeffe, *in* "Superionic Conductors" (G. D. Mahan and W. L. Roth, Eds.), p. 101, Plenum, Press, New York (1976).
7. A. V. Chadwick, *Solid State Ionics* **8,** 209 (1983).
8. R. Kanno, Y. Takeda, O. Yamamoto, C. Cros, Wang Gang, and P. Hagenmuller, *Solid State Ionics* **20,** 99 (1986); J. L. Soubeyroux, C. Cros, Wang Gang, R. Kanno, and M. Pouchard, *Solid State Ionics* **15,** 293 (1985).
9. S. Geller and B. B. Owens, *J. Phys. Chem. Solids* **33,** 1241 (1972).
10. Xue Rong-Jian, Yao-Shu, Zhao Zong-Yuana, and Chen Li-Quan, *Acta Phys. Sin.* **31,** 810 (1982).
11. Zhao Zong-Yuan, Chen Li-Quan, Ni Yong-Ming, and Ma Ming-Rong, *Acta Phys. Sin.* **33,** 1556 (1984).
12. A. Turkovic and D. Sokcevic, *Solid State Ionics* **28–30,** 276 (1988).
13. T. Atake, H. Kawaji, R. Kanno, K. Ohno, and O. Yamamoto, *Solid State Ionics* **53/56,** 1260 (1992).
14. F. Izumi, *J. Mineral. Soc. Japan* **17,** 37 (1985). [in Japanese]
15. N. Watanabe, H. Asano, H. Iwasa, S. Satoi H. Murata, K. Karahashi, S. Tomiyoshi, F Izumi, and K. Inoue, *Japn. J. Appl. Phys.* **26** 1164 (1987).
16. T. Takahashi, R. Kanno, Y. Takeda, and O. Yamamoto, *Solid State Ionics* **3/4,** 283 (1981).
17. M. Tokumoto, N. Ohnishi, Y. Okada, and T. Ishiguro. *Solid State Ionics* **3/4,** 289 (1981).
18. S. Geller, K. Nag, and A. K. Ray, *J. Electrochem. Soc.* **128,** 2670 (1981).
19. R. Kanno, Y. Takeda, M. Imura, and O. Yamamoto, *J. Appl. Electrochem.* **12,** 681 (1982).
20. M. Kleitz, J. R. Akridge, and J. H. Kennedy, *Solid State Ionics* **2,** 67 (1981).
21. S. Geller, K. Nag, and A. K. Ray, *J. Electrochem. Soc.* **128,** 2675 (1981).
22. R. A. Young, E. Prince, and R. A. Sparks, *J. Appl. Crystallogr.* **15,** 357 (1982).
23. W. R. Busing, K. O. Martin, and H. A. Levy, Report ORNL-TM-306, Oak Ridge National Laboratory, Oak Ridge, TN (1964).
24. S. Geller, *Science* **157,** 310 (1967).
25. A. Yamamoto and F. Izumi, private communication (1988).
26. See, e.g., J. M. Ziman, "Principles of the Theory of Solids," 2nd ed., pp. 37–42, Cambridge Univ. Press, London, (1972).